Modular Discontinuous Galerkin Time-Domain Method for General Dispersive Media With Vector Fitting

Tiago V. L. Amorim, *Member, IEEE*, Elson J. Silva, Fernando J. S. Moreira, and Fernando L. Teixeira

***Abstract*—We present a novel modular implementation of the discontinuous Galerkin time-domain (DGTD) method to effectively address electromagnetic problems involving general dielectric dispersive media modeled through vector fitting. This approach includes an extended dispersive perfectly matched layer to directly truncate dispersive materials, allowing for the modeling of open domains. The proposed modular and concise DGTD implementation, based on the complex-conjugate pole-residue model, offers flexibility and simplifies the handling of complex medium problems. We apply the formulation to both two-dimensional and three-dimensional canonical scattering problems, demonstrating good agreement with their respective analytical solutions.**

***Index Terms*—Scattering, dispersive media, discontinuous Galerkin time-domain.**

I. Introduction

THE DGTD method offers an effective approach for solving electromagnetic problems, particularly in scattering, wave propagation, and antenna analysis [1], [2], [3], [4], [5]. It combines the geometric flexibility of the finite-element method (FEM) [6] with, to some extent, the versatility of explicit time integration of the finite-difference time-domain (FDTD) method [7].

In this work, the standard DGTD framework for solving Maxwell's equations [8] is extended to handle general dielectric dispersive media modeled by the complex-conjugate pole-residue (CCPR) model [9] and to incorporate a *dispersive* perfectly matched layer (PML) absorbing boundary condition in a modular way. Unlike earlier approaches based on Padé approximants that rely on scattering boundary condition (SBC) for domain truncation [10] or demand extra space between the scatterer and the PML [11], the proposed DGTD formulation is a generalization of [12] that allows for direct truncation of dispersive materials without any additional free space. It incorporates a general dielectric dispersive CCPR model [13] while extending the uniaxial PML [14] to match general dispersive media, enabling efficient simulation of open space [15].

This formulation first solves the standard Maxwell equations across the entire domain, providing a unified baseline. Additional terms, such as those for PML or dispersive media modeled using vector fitting [16], are then selectively added through the auxiliary differential equation (ADE) approach, in a plug-and-play fashion. Depending on each region's characteristics—dispersive media, simple dielectric PML, or dispersive PML—additional differential equations and correction terms are incorporated as needed (see Fig. 1). This modular approach activates specific extensions only in targeted regions, enabling efficient batch processing and scalable computation. The careful definition of ADE terms, particularly for boundary conditions in dispersive media, ensures the algorithm remains adaptable and modular.

The main advantage of this approach is its modularity, combined with the ability to directly truncate general dispersive media without any additional free space. It is particularly beneficial for wideband problems [17], [18], [19] in open domains, where multiple dispersion terms are required to capture material behavior across a broad frequency range efficiently.

Additionally, incident fields are naturally incorporated using the total-field scattered-field (TFSF) formulation [7]. Numerical validation is performed by comparing the DGTD solutions of two-dimensional and three-dimensional canonical scattering problems with their analytical counterparts.

II. Mathematical Formulation

Maxwell's curl equations for lossless linear media without sources [6] are written as

$$\bar{\bar{\mu}}(\boldsymbol{r})\frac{\partial \boldsymbol{\mathcal{H}}(\boldsymbol{r},t)}{\partial t}+\nabla\times\boldsymbol{\mathcal{E}}(\boldsymbol{r},t)=0, \tag{1}$$

$$\bar{\bar{\epsilon}}(\boldsymbol{r})\frac{\partial \boldsymbol{\mathcal{E}}(\boldsymbol{r},t)}{\partial t}-\nabla\times\boldsymbol{\mathcal{H}}(\boldsymbol{r},t)=0, \tag{2}$$

where $\boldsymbol{\mathcal{E}}$ and $\boldsymbol{\mathcal{H}}$ are the electric and magnetic fields in the time domain, respectively. Additionally, $\bar{\bar{\epsilon}}$ and $\bar{\bar{\mu}}$ are the electric permittivity and the magnetic permeability tensors, respectively.

Received 21 November 2024; revised 2 February 2025; accepted 9 February 2025. Date of publication 17 February 2025; date of current version 25 March 2025. This work was supported by CNPq and CAPES-PROEX, Brazil. *(Corresponding author: Tiago V. L. Amorim.)*

Tiago V. L. Amorim is with the Graduate Program in Electrical Engineering, Federal University of Minas Gerais, Belo Horizonte, MG 31270-901, Brazil (e-mail: tiagovla@ufmg.br).

Elson J. Silva is with the Department of Electrical Engineering, Federal University of Minas Gerais, Belo Horizonte, MG 31270-901, Brazil (e-mail: elson@cpdee.ufmg.br).

Fernando J. S. Moreira is with the Department of Electronic Engineering, Federal University of Minas Gerais, Belo Horizonte, MG 31270-901, Brazil (e-mail: fernando@eee.ufmg.br).

Fernando L. Teixeira is with the ElectroScience Laboratory, The Ohio State University, Columbus, OH 43212 USA (e-mail: teixeira.5@osu.edu).

Digital Object Identifier 10.1109/JMMCT.2025.3542379

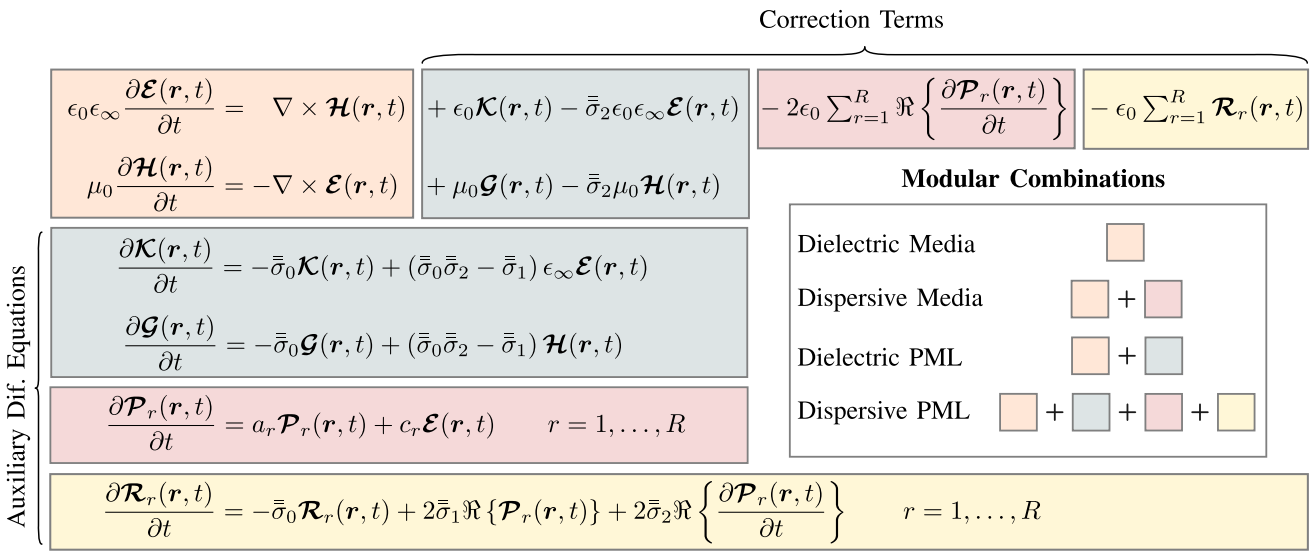

Fig. 1. Illustration of the modular implementation of Maxwell's equations containing dispersive media truncated by dispersive PML. The system of equations is solved synchronously, with each timestep iteration computing the right-hand side (RHS) numerically. Initially, Maxwell's equations for dielectric media are computed across the entire computational domain using the respective nodal fields $\mathcal{E}$ and $\mathcal{H}$ (highlighted in orange). If the region is dispersive, additional auxiliary fields $\mathcal{P}_r$ are added *in place* to the right-hand side (RHS), updating the previously calculated values for that region based on their respective ADE (highlighted in red). In regions with dielectric PML, the RHS is updated *in place* with terms involving the nodal fields $\mathcal{G}$ and $\mathcal{K}$, which are calculated using their respective ADEs (highlighted in gray). In regions with dispersive PML, the updates for both dispersive media and dielectric PML are combined, introducing an additional coupling $\mathcal{R}_r$ (highlighted in yellow). Auxiliary fields are defined only when needed, and region updates are performed via array indexing.

Furthermore, $\boldsymbol{r}$ and t indicate the spatial and temporal dependencies, respectively.

In conservation form, the aforementioned equations become [20]

$$\boldsymbol{Q}(\boldsymbol{r})\frac{\partial \vec{q}(\boldsymbol{r},t)}{\partial t} + \nabla \cdot \vec{\boldsymbol{\mathcal{F}}}(\vec{q},\boldsymbol{r},t) = 0, \tag{3}$$

where

$$\vec{q}(\boldsymbol{r},t) = \begin{bmatrix} \boldsymbol{\mathcal{H}}(\boldsymbol{r},t) \\ \boldsymbol{\mathcal{E}}(\boldsymbol{r},t) \end{bmatrix}, \qquad \boldsymbol{Q}(\boldsymbol{r}) = \begin{bmatrix} \bar{\bar{\mu}}(\boldsymbol{r}) & 0 \\ 0 & \bar{\bar{\epsilon}}(\boldsymbol{r}) \end{bmatrix},$$

$$\vec{\boldsymbol{\mathcal{F}}}(\vec{q}) = \left[\vec{\mathcal{F}}_1, \vec{\mathcal{F}}_2, \vec{\mathcal{F}}_3\right]^{\mathsf{T}}, \qquad \vec{\mathcal{F}}_i(\vec{q}) = \begin{bmatrix} \boldsymbol{e}_i \times \boldsymbol{\mathcal{E}}(\boldsymbol{r},t) \\ -\boldsymbol{e}_i \times \boldsymbol{\mathcal{H}}(\boldsymbol{r},t) \end{bmatrix},$$

with $\vec{\boldsymbol{\mathcal{F}}}$ being the flux and $\boldsymbol{e}_i$ representing the three Cartesian unit vectors for $i = 1, 2, 3$. For simplicity, any medium in this work is considered isotropic with $\bar{\bar{\epsilon}} = \epsilon \boldsymbol{I}$ and $\bar{\bar{\mu}} = \mu \boldsymbol{I}$, where $\boldsymbol{I}$ is the identity matrix.

A. Dispersive Media Modeling

A general dispersive dielectric material can be modeled by considering its permittivity $\epsilon(\omega)$ as $\epsilon_0\epsilon_\infty + \epsilon_0\chi_e(\omega)$, where ϵ_∞ is the high frequency relative permittivity limit and $\chi_e(\omega)$ is the frequency-dependent electric susceptibility. Specifically, using the CCPR model [9], $\chi_e(\omega)$ can be expanded as

$$\chi_e(\omega) = \sum_{r=1}^{R}\left(\frac{c_r}{j\omega - a_r} + \frac{c_r^*}{j\omega - a_r^*}\right), \tag{4}$$

where R is the number of poles, c_r and a_r are the model's parameters obtained from data fitting.

This dispersion model can be incorporated via the electric constitutive equation as

$$j\omega \boldsymbol{D}(\boldsymbol{r},\omega) = j\omega\epsilon_0\epsilon_\infty \boldsymbol{E}(\boldsymbol{r},\omega) + j\omega\epsilon_0\chi_e(\omega)\boldsymbol{E}(\boldsymbol{r},\omega). \tag{5}$$

The aforementioned equation can be decomposed into the following system of equations

$$j\omega \boldsymbol{D}(\boldsymbol{r},\omega) = j\omega\epsilon_0\epsilon_\infty \boldsymbol{E}(\boldsymbol{r},\omega) + \epsilon_0 \boldsymbol{K}(\boldsymbol{r},\omega), \tag{6}$$

$$\boldsymbol{K}(\boldsymbol{r},\omega) = j\omega\chi_e(\boldsymbol{r},\omega)\boldsymbol{E}(\boldsymbol{r},\omega). \tag{7}$$

By introducing the following definitions

$$\boldsymbol{P}_r(\boldsymbol{r},\omega) = \frac{c_r}{j\omega - a_r}\boldsymbol{E}(\boldsymbol{r},\omega), \tag{8}$$

$$\boldsymbol{P}'_r(\boldsymbol{r},\omega) = \frac{c_r^*}{j\omega - a_r^*}\boldsymbol{E}(\boldsymbol{r},\omega), \tag{9}$$

where both of them can be easily converted back to the time domain as

$$\frac{\partial \boldsymbol{\mathcal{P}}_r(\boldsymbol{r},t)}{\partial t} - a_r \boldsymbol{\mathcal{P}}_r(\boldsymbol{r},t) = c_r \boldsymbol{\mathcal{E}}(\boldsymbol{r},t), \tag{10}$$

$$\frac{\partial \boldsymbol{\mathcal{P}}'_r(\boldsymbol{r},t)}{\partial t} - a_r^* \boldsymbol{\mathcal{P}}'_r(\boldsymbol{r},t) = c_r^* \boldsymbol{\mathcal{E}}(\boldsymbol{r},t), \tag{11}$$

Equation (7) can be rewritten as

$$\boldsymbol{K}(\boldsymbol{r},\omega) = j\omega \sum_{r=1}^{R}\left(\boldsymbol{P}_r(\boldsymbol{r},\omega) + \boldsymbol{P}'_r(\boldsymbol{r},\omega)\right). \tag{12}$$

Since $\boldsymbol{\mathcal{E}}(\boldsymbol{r},t) \in \mathbb{R}$, it implies that $\boldsymbol{\mathcal{P}}_r'(\boldsymbol{r},t) = \boldsymbol{\mathcal{P}}_r^*(\boldsymbol{r},t)$, resulting in its time-domain equation to be

$$\boldsymbol{\mathcal{K}}(\boldsymbol{r},t) = 2\sum_{r=1}^{R} \Re\left\{\frac{\partial \boldsymbol{\mathcal{P}}_r(\boldsymbol{r},t)}{\partial t}\right\}, \tag{13}$$

with only one of ADEs (10) or (11) needing to be solved. Therefore, within a dispersive material, (2) becomes

$$\nabla \times \boldsymbol{\mathcal{H}}(\boldsymbol{r},t) = \epsilon_0\epsilon_\infty \frac{\partial \boldsymbol{\mathcal{E}}(\boldsymbol{r},t)}{\partial t} - 2\epsilon_0 \sum_{r=1}^{R} \Re\left\{\frac{\partial \boldsymbol{\mathcal{P}}_r(\boldsymbol{r},t)}{\partial t}\right\}, \tag{14}$$

and an additional ADE of a polarization field $\boldsymbol{\mathcal{P}}_r$ for every pole r is solved

$$\frac{\partial \boldsymbol{\mathcal{P}}_r(\boldsymbol{r},t)}{\partial t} = a_r \boldsymbol{\mathcal{P}}_r(\boldsymbol{r},t) + c_r \boldsymbol{\mathcal{E}}(\boldsymbol{r},t). \tag{15}$$

B. Perfectly Matched Layer

To truncate unbounded domains, the uniaxial PML [14] technique can be used by introducing matched artificial conductivities in the outer regions of the grid to absorb outgoing waves. This PML is incorporated by modifying the electrical constitutive equation to

$$j\omega \boldsymbol{D}(\boldsymbol{r},\omega) = j\omega \bar{\bar{\Lambda}} \epsilon_0\epsilon_\infty \boldsymbol{E}(\boldsymbol{r},\omega), \tag{16}$$

where the tensor $\bar{\bar{\Lambda}}$ is defined as

$$\bar{\bar{\Lambda}} = \begin{bmatrix} s_y s_z/s_x & 0 & 0 \\ 0 & s_x s_z/s_y & 0 \\ 0 & 0 & s_x s_y/s_z \end{bmatrix}, \tag{17}$$

with $s_i = 1 + \sigma_i/j\omega$ for $i = x, y, z$. Equation (16) can be rewritten as [21]

$$\begin{aligned} j\omega \boldsymbol{D}(\boldsymbol{r},\omega) &= j\omega\epsilon_0\epsilon_\infty \boldsymbol{E}(\boldsymbol{r},\omega) \\ &\quad + j\omega \left(\bar{\bar{\Lambda}} - \boldsymbol{I}\right) \epsilon_0\epsilon_\infty \boldsymbol{E}(\boldsymbol{r},\omega), \end{aligned} \tag{18}$$

which it can be further decomposed into the following set of equations

$$j\omega \boldsymbol{D}(\boldsymbol{r},\omega) = j\omega\epsilon_0\epsilon_\infty \boldsymbol{E}(\boldsymbol{r},\omega) + \epsilon_0 \boldsymbol{U}(\boldsymbol{r},\omega), \tag{19}$$

$$\boldsymbol{U}(\boldsymbol{r},\omega) = j\omega(\bar{\bar{\Lambda}} - \boldsymbol{I})\epsilon_\infty \boldsymbol{E}(\boldsymbol{r},\omega). \tag{20}$$

By defining the following coefficients

$$\bar{\bar{\sigma}}_0 = \begin{bmatrix} \sigma_x & 0 & 0 \\ 0 & \sigma_y & 0 \\ 0 & 0 & \sigma_z \end{bmatrix}, \quad \bar{\bar{\sigma}}_1 = \begin{bmatrix} \sigma_y\sigma_z & 0 & 0 \\ 0 & \sigma_x\sigma_z & 0 \\ 0 & 0 & \sigma_x\sigma_y \end{bmatrix},$$

$$\bar{\bar{\sigma}}_2 = \begin{bmatrix} \sigma_y + \sigma_z - \sigma_x & 0 & 0 \\ 0 & \sigma_x + \sigma_z - \sigma_y & 0 \\ 0 & 0 & \sigma_x + \sigma_y - \sigma_z \end{bmatrix},$$

Equation (20) can be expanded to

$$\begin{aligned} \bar{\bar{\sigma}}_0 \boldsymbol{U}(\boldsymbol{r},\omega) &= \bar{\bar{\sigma}}_1 \epsilon_\infty \boldsymbol{E}(\boldsymbol{r},\omega) \\ &\quad + j\omega \left[-\boldsymbol{U}(\boldsymbol{r},\omega) + \bar{\bar{\sigma}}_2 \epsilon_\infty \boldsymbol{E}(\boldsymbol{r},\omega)\right]. \end{aligned} \tag{21}$$

The following substitution

$$\boldsymbol{K}(\boldsymbol{r},\omega) = -\boldsymbol{U}(\boldsymbol{r},\omega) + \bar{\bar{\sigma}}_2 \epsilon_\infty \boldsymbol{E}(\boldsymbol{r},\omega), \tag{22}$$

results in the following equation after some simplifications

$$j\omega \boldsymbol{K}(\boldsymbol{r},\omega) = -\bar{\bar{\sigma}}_0 \boldsymbol{K}(\boldsymbol{r},\omega) + \left(\bar{\bar{\sigma}}_0\bar{\bar{\sigma}}_2 - \bar{\bar{\sigma}}_1\right)\epsilon_\infty \boldsymbol{E}(\boldsymbol{r},\omega), \tag{23}$$

which in the time domain simply becomes

$$\frac{\partial \boldsymbol{\mathcal{K}}(\boldsymbol{r},t)}{\partial t} = -\bar{\bar{\sigma}}_0 \boldsymbol{\mathcal{K}}(\boldsymbol{r},t) + \left(\bar{\bar{\sigma}}_0\bar{\bar{\sigma}}_2 - \bar{\bar{\sigma}}_1\right)\epsilon_\infty \boldsymbol{\mathcal{E}}(\boldsymbol{r},t). \tag{24}$$

The same procedure can be applied to the magnetic field, resulting in the following ADE

$$\frac{\partial \boldsymbol{\mathcal{G}}(\boldsymbol{r},t)}{\partial t} = -\bar{\bar{\sigma}}_0 \boldsymbol{\mathcal{G}}(\boldsymbol{r},t) + \left(\bar{\bar{\sigma}}_0\bar{\bar{\sigma}}_2 - \bar{\bar{\sigma}}_1\right) \boldsymbol{\mathcal{H}}(\boldsymbol{r},t). \tag{25}$$

Finally, the set of equations to be solved within the uniaxial PML is given by

$$\nabla \times \boldsymbol{\mathcal{H}}(\boldsymbol{r},t) = \epsilon_0\epsilon_\infty \frac{\partial \boldsymbol{\mathcal{E}}(\boldsymbol{r},t)}{\partial t} - \epsilon_0 \boldsymbol{\mathcal{K}}(\boldsymbol{r},t) + \bar{\bar{\sigma}}_2 \epsilon_0\epsilon_\infty \boldsymbol{\mathcal{E}}(\boldsymbol{r},t), \tag{26}$$

$$\nabla \times \boldsymbol{\mathcal{E}}(\boldsymbol{r},t) = -\mu_0 \frac{\partial \boldsymbol{\mathcal{H}}(\boldsymbol{r},t)}{\partial t} - \mu_0 \boldsymbol{\mathcal{G}}(\boldsymbol{r},t) + \bar{\bar{\sigma}}_2 \mu_0 \boldsymbol{\mathcal{H}}(\boldsymbol{r},t), \tag{27}$$

$$\frac{\partial \boldsymbol{\mathcal{K}}(\boldsymbol{r},t)}{\partial t} = -\bar{\bar{\sigma}}_0 \boldsymbol{\mathcal{K}}(\boldsymbol{r},t) + \left(\bar{\bar{\sigma}}_0\bar{\bar{\sigma}}_2 - \bar{\bar{\sigma}}_1\right)\epsilon_\infty \boldsymbol{\mathcal{E}}(\boldsymbol{r},t), \tag{28}$$

$$\frac{\partial \boldsymbol{\mathcal{G}}(\boldsymbol{r},t)}{\partial t} = -\bar{\bar{\sigma}}_0 \boldsymbol{\mathcal{G}}(\boldsymbol{r},t) + \left(\bar{\bar{\sigma}}_0\bar{\bar{\sigma}}_2 - \bar{\bar{\sigma}}_1\right) \boldsymbol{\mathcal{H}}(\boldsymbol{r},t). \tag{29}$$

C. PML Matched to General Dispersive Media

In order to properly truncate dispersive media, it is necessary to incorporate the PML equations in tandem with the dispersive medium model. In this case, the electric constitutive equation becomes

$$j\omega \boldsymbol{D}(\boldsymbol{r},\omega) = j\omega \left[\boldsymbol{I} + \left(\bar{\bar{\Lambda}} - \boldsymbol{I}\right)\right] \epsilon_0 \left(\epsilon_\infty + \chi_e(\boldsymbol{r},\omega)\right) \boldsymbol{E}(\boldsymbol{r},\omega). \tag{30}$$

Expanding the previous equation leads to

$$\begin{aligned} j\omega \boldsymbol{D}(\boldsymbol{r},\omega) &= \overbrace{j\omega\epsilon_0\epsilon_\infty \boldsymbol{E}(\boldsymbol{r},\omega)}^{\text{simple dielectric}} + \overbrace{j\omega(\bar{\bar{\Lambda}} - \boldsymbol{I})\epsilon_0\epsilon_\infty \boldsymbol{E}(\boldsymbol{r},\omega)}^{\text{simple PML}} \\ &\quad + \underbrace{j\omega\epsilon_0\chi_e(\boldsymbol{r},\omega)\boldsymbol{E}(\boldsymbol{r},\omega)}_{\text{dispersive media}} + \underbrace{j\omega(\bar{\bar{\Lambda}} - \boldsymbol{I})\epsilon_0\chi_e(\boldsymbol{r},\omega)\boldsymbol{E}(\boldsymbol{r},\omega)}_{\text{coupling: PML + dispersive media}} \end{aligned} \tag{31}$$

where the simple dielectric, the dispersive media, and the simple PML terms have already been addressed in the previous subsections. Therefore, we focus next on the remaining coupling term.

By writing (31) as the following set of equations

$$\begin{aligned} j\omega \boldsymbol{D}(\boldsymbol{r},\omega) &= j\omega\epsilon_0\epsilon_\infty \boldsymbol{E}(\boldsymbol{r},\omega) + j\omega\epsilon_0\chi_e(\boldsymbol{r},\omega)\boldsymbol{E}(\boldsymbol{r},\omega) \\ &\quad + j\omega(\bar{\bar{\Lambda}} - \boldsymbol{I})\epsilon_0\epsilon_\infty \boldsymbol{E}(\boldsymbol{r},\omega) + \epsilon_0 \boldsymbol{R}(\boldsymbol{r},\omega), \end{aligned} \tag{32}$$

$$\boldsymbol{R}(\boldsymbol{r},\omega) = j\omega(\bar{\bar{\Lambda}} - \boldsymbol{I})\chi_e(\boldsymbol{r},\omega)\boldsymbol{E}(\boldsymbol{r},\omega), \tag{33}$$

and considering the subsequent definition

$$\boldsymbol{R}(\boldsymbol{r},\omega)=\sum_{r=1}^{R}\boldsymbol{R}_r(\boldsymbol{r},\omega), \tag{34}$$

Equation (33) can be rewritten as a sum of ADEs associated to each pole r as

$$\begin{aligned} j\omega\boldsymbol{R}_r(\boldsymbol{r},\omega) = &-\bar{\bar{\sigma}}_0\boldsymbol{R}_r(\boldsymbol{r},\omega) \\ &+\left(j\omega\bar{\bar{\sigma}}_2+\bar{\bar{\sigma}}_1\right)\left(\boldsymbol{P}_r(\boldsymbol{r},\omega)+\boldsymbol{P}'_r(\boldsymbol{r},\omega)\right) \end{aligned} \tag{35}$$

with its time-domain counterpart being

$$\begin{aligned} \frac{\partial\boldsymbol{\mathcal{R}}_r(\boldsymbol{r},t)}{\partial t} = &-\bar{\bar{\sigma}}_0\boldsymbol{\mathcal{R}}_r(\boldsymbol{r},t) \\ &+2\bar{\bar{\sigma}}_1\Re\left\{\boldsymbol{\mathcal{P}}_r(\boldsymbol{r},t)\right\}+2\bar{\bar{\sigma}}_2\Re\left\{\frac{\partial\boldsymbol{\mathcal{P}}_r(\boldsymbol{r},t)}{\partial t}\right\}. \end{aligned} \tag{36}$$

Therefore, the set of equations to be solved is

$$\begin{aligned} \epsilon_0\epsilon_\infty\frac{\partial\boldsymbol{\mathcal{E}}(\boldsymbol{r},t)}{\partial t} = &\nabla\times\boldsymbol{\mathcal{H}}(\boldsymbol{r},t)+\epsilon_0\boldsymbol{\mathcal{K}}(\boldsymbol{r},t)-\bar{\bar{\sigma}}_2\epsilon_0\epsilon_\infty\boldsymbol{\mathcal{E}}(\boldsymbol{r},t) \\ &-2\epsilon_0\sum_{r=1}^{R}\Re\left\{\frac{\partial\boldsymbol{\mathcal{P}}_r(\boldsymbol{r},t)}{\partial t}\right\}-\epsilon_0\sum_{r=1}^{R}\boldsymbol{\mathcal{R}}_r(\boldsymbol{r},t), \end{aligned} \tag{37}$$

$$\mu_0\frac{\partial\boldsymbol{\mathcal{H}}(\boldsymbol{r},t)}{\partial t}=-\nabla\times\boldsymbol{\mathcal{E}}(\boldsymbol{r},t)+\mu_0\boldsymbol{\mathcal{G}}(\boldsymbol{r},t)-\bar{\bar{\sigma}}_2\mu_0\boldsymbol{\mathcal{H}}(\boldsymbol{r},t), \tag{38}$$

$$\frac{\partial\boldsymbol{\mathcal{K}}(\boldsymbol{r},t)}{\partial t}=-\bar{\bar{\sigma}}_0\boldsymbol{\mathcal{K}}(\boldsymbol{r},t)+\left(\bar{\bar{\sigma}}_0\bar{\bar{\sigma}}_2-\bar{\bar{\sigma}}_1\right)\epsilon_\infty\boldsymbol{\mathcal{E}}(\boldsymbol{r},t), \tag{39}$$

$$\frac{\partial\boldsymbol{\mathcal{G}}(\boldsymbol{r},t)}{\partial t}=-\bar{\bar{\sigma}}_0\boldsymbol{\mathcal{G}}(\boldsymbol{r},t)+\left(\bar{\bar{\sigma}}_0\bar{\bar{\sigma}}_2-\bar{\bar{\sigma}}_1\right)\boldsymbol{\mathcal{H}}(\boldsymbol{r},t), \tag{40}$$

$$\frac{\partial\boldsymbol{\mathcal{P}}_r(\boldsymbol{r},t)}{\partial t}=a_r\boldsymbol{\mathcal{P}}_r(\boldsymbol{r},t)+c_r\boldsymbol{\mathcal{E}}(\boldsymbol{r},t),\quad r=1,\ldots,R, \tag{41}$$

$$\begin{aligned} \frac{\partial\boldsymbol{\mathcal{R}}_r(\boldsymbol{r},t)}{\partial t} = &-\bar{\bar{\sigma}}_0\boldsymbol{\mathcal{R}}_r(\boldsymbol{r},t)+2\bar{\bar{\sigma}}_2\Re\left\{\frac{\partial\boldsymbol{\mathcal{P}}_r(\boldsymbol{r},t)}{\partial t}\right\} \\ &+2\bar{\bar{\sigma}}_1\Re\left\{\boldsymbol{\mathcal{P}}_r(\boldsymbol{r},t)\right\}\quad r=1,\ldots,R. \end{aligned} \tag{42}$$

D. Modular Implementation

An examination of all possible scenarios makes it evident that the (simple) dielectric case, (1) and (2), the dispersive media case, (1), (14) and (15), and the dielectric PML case, (26) to (29), are just specific instances of the more general dispersive PML case, (37) to (42). Notably, while the (simple) dielectric media case can be computed for the entire domain directly, other regions only require respective additional terms according to their specific characteristics. This modular approach is illustrated in Fig. 1.

III. The Discontinous Galerkin Method

Assume that Ω_h is a tessellated finite region (bounded by $\partial\Omega_h$) of the physical domain Ω with K non-overlapping elements (Ω_h^k, bounded by $\partial\Omega_h^k$) where (3) is to be solved. Thus

$$\Omega\approx\Omega_h=\bigcup_{k}^{K}\Omega_h^k. \tag{43}$$

A globally defined vector space $\mathcal{V}_h$ is introduced to approximate $\vec{q}(\boldsymbol{r},t)$ given that $\mathcal{V}_h=\oplus_{k=1}^{K}\mathcal{V}_h^k$, where the locally defined vector spaces are defined as $\mathcal{V}_h^k=\text{span}\{\psi_n(\Omega_h^k)\}_{n=1}^{N_p}$. Considering that $\mathcal{V}_h$ is piecewise smooth over Ω_h, a local approximation $\vec{q}_h^k(\boldsymbol{r},t)$ is defined in the local vector space $\mathcal{V}_h$ [8]

$$\vec{q}_h^k(\boldsymbol{r},t)=\sum_{n=1}^{N_p}\vec{\tilde{q}}_n^k(t)\cdot\psi_n(\boldsymbol{r})=\sum_{i=1}^{N_p}\vec{\tilde{q}}_h^k(\boldsymbol{r},t)\cdot l_i(\boldsymbol{r})\quad \boldsymbol{r}\in\Omega^k, \tag{44}$$

where l_i are the interpolating Lagrange nodal-basis which possess the Kronecker delta property [21]. The relation between modal coefficients $\vec{\tilde{q}}_n^k(t)$ and nodal coefficients $\vec{\tilde{q}}_h^k(\boldsymbol{r},t)$ is given by the Vandermonde matrix [8]. The modal-basis are usually chosen to be normalized monomials, while the interpolating positions $\boldsymbol{r}$ are spread in a Gauss-Lobatto alike distribution, usually obtained by the Warp-Blend method [8].

By applying the Galerkin testing and local integration by parts over (3) for each element, the strong variational formulation of Maxwell's curl equations [21] writes as

$$\begin{aligned} &\int_{\Omega_h^k}\left[Q\frac{\partial\vec{q}_h^k}{\partial t}+\nabla\cdot\vec{\boldsymbol{\mathcal{F}}}_h^k(\vec{q}_h^k)\right]\cdot l_i(\boldsymbol{r})\,d\Omega \\ &=\int_{\partial\Omega_h^k}\hat{\boldsymbol{n}}\cdot\left[\vec{\boldsymbol{\mathcal{F}}}_h^k(\vec{q}_h^k)-\vec{\boldsymbol{\mathcal{F}}}^*(\vec{q}_h^k)\right]\cdot l_i(\boldsymbol{r})\,d\Omega\quad\forall l_i\in\mathcal{V}_h^k, \end{aligned} \tag{45}$$

where $\hat{\boldsymbol{n}}$ is the outward unit vector normal to the boundary surface $\partial\Omega_h^k$ and $\mathcal{F}_h^k-\mathcal{F}^*$ are termed as the numerical flux difference used for inter-element coupling.

Within each element, the physical fields $\boldsymbol{\mathcal{E}}(\boldsymbol{r},t)$ and $\boldsymbol{\mathcal{H}}(\boldsymbol{r},t)$ are approximated by $\boldsymbol{\mathcal{E}}_h^k(\boldsymbol{r},t)$ and $\boldsymbol{\mathcal{H}}_h^k(\boldsymbol{r},t)$ using nodal basis functions as

$$\boldsymbol{\mathcal{E}}_h^k(\boldsymbol{r},t)=\sum_{i=1}^{N_p}\tilde{\boldsymbol{e}}_h^k(\boldsymbol{r}_i,t)\cdot l_i(\boldsymbol{r})\qquad\boldsymbol{r}\in\Omega_h^k, \tag{46}$$

$$\boldsymbol{\mathcal{H}}_h^k(\boldsymbol{r},t)=\sum_{i=1}^{N_p}\tilde{\boldsymbol{h}}_h^k(\boldsymbol{r}_i,t)\cdot l_i(\boldsymbol{r})\qquad\boldsymbol{r}\in\Omega_h^k, \tag{47}$$

where $\tilde{\boldsymbol{e}}_h^k$ and $\tilde{\boldsymbol{h}}_h^k$ are the nodal coefficients. After replacing (46) and (47) into (45) and assuming that Q in (3) is constant within each element for simplicity, the integrals simplify to

$$M_{ij}^k=\int_{\Omega_h^k}l_i(\boldsymbol{r})\cdot l_j(\boldsymbol{r})\,d\Omega, \tag{48}$$

$$S_{ij,s}^k=\int_{\Omega_h^k}l_i(\boldsymbol{r})\cdot\frac{\partial l_j(\boldsymbol{r})}{\partial s}\,d\Omega\quad s=x,y,z, \tag{49}$$

$$F_{ij,f}^k=\int_{\partial\Omega_h^k}l_i(\boldsymbol{r})\cdot l_j(\boldsymbol{r})\,d\Omega, \tag{50}$$

where M^k is the mass matrix, S_s^k is the stiffness matrix along the s component, and F_f^k is the face mass matrix for face f. By

isolating the time-derivatives and approximating the fields $\mathcal{K}$, $\mathcal{G}$, $\mathcal{P}$, $\mathcal{R}$ in a similar fashion as in (46) and (47), one obtains

$$\epsilon_0\epsilon_\infty^k\frac{\partial\tilde{\boldsymbol{e}}^k}{\partial t}=\left(M^k\right)^{-1}\cdot\left[\boldsymbol{S}^k\times\tilde{\boldsymbol{h}}^k+F_f^k\cdot\left(\hat{\boldsymbol{n}}\cdot\left[\vec{\boldsymbol{\mathcal{F}}}_E^k-\vec{\boldsymbol{\mathcal{F}}}_E^*\right]\right)\right]+\epsilon_0\tilde{\boldsymbol{k}}^k-\bar{\bar{\sigma}}_2\epsilon_0\epsilon_\infty^k\tilde{\boldsymbol{e}}^k-2\epsilon_0\sum_{r=1}^{R}\Re\left\{\frac{\partial\tilde{\boldsymbol{p}}_r^k}{\partial t}\right\}-\epsilon_0\sum_{r=1}^{R}\tilde{\boldsymbol{r}}_r, \tag{51}$$

$$\mu_0\frac{\partial\tilde{\boldsymbol{h}}^k}{\partial t}=\left(M^k\right)^{-1}\cdot\left[-\boldsymbol{S}^k\times\tilde{\boldsymbol{e}}^k+F_f^k\cdot\left(\hat{\boldsymbol{n}}\cdot\left[\vec{\boldsymbol{\mathcal{F}}}_H^k-\vec{\boldsymbol{\mathcal{F}}}_H^*\right]\right)\right]+\mu_0\tilde{\boldsymbol{g}}^k-\bar{\bar{\sigma}}_2\mu_0\tilde{\boldsymbol{h}}^k, \tag{52}$$

$$\frac{\partial\tilde{\boldsymbol{k}}^k}{\partial t}=-\bar{\bar{\sigma}}_0\tilde{\boldsymbol{k}}^k+\left(\bar{\bar{\sigma}}_0\bar{\bar{\sigma}}_2-\bar{\bar{\sigma}}_1\right)\epsilon_\infty\tilde{\boldsymbol{e}}^k, \tag{53}$$

$$\frac{\partial\tilde{\boldsymbol{g}}^k}{\partial t}=-\bar{\bar{\sigma}}_0\tilde{\boldsymbol{g}}^k+\left(\bar{\bar{\sigma}}_0\bar{\bar{\sigma}}_2-\bar{\bar{\sigma}}_1\right)\tilde{\boldsymbol{h}}^k, \tag{54}$$

$$\frac{\partial\tilde{\boldsymbol{p}}_r^k}{\partial t}=a_r\tilde{\boldsymbol{p}}_r^k+c_r\tilde{\boldsymbol{e}}^k\quad r=1,\ldots,R, \tag{55}$$

$$\frac{\partial\tilde{\boldsymbol{r}}_r^k}{\partial t}=-\bar{\bar{\sigma}}_0\tilde{\boldsymbol{r}}_r^k+2\bar{\bar{\sigma}}_2\Re\left\{\frac{\partial\tilde{\boldsymbol{p}}_r^k}{\partial t}\right\}+2\bar{\bar{\sigma}}_1\Re\left\{\tilde{\boldsymbol{p}}_r^k\right\}\quad r=1,\ldots,R, \tag{56}$$

where $\boldsymbol{S}^k=[S_x^k,S_y^k,S_z^k]^\intercal$, and $\vec{\boldsymbol{\mathcal{F}}}_E$ and $\vec{\boldsymbol{\mathcal{F}}}_H$ are the fluxes related to the electric and magnetic field, respectively.

A. Numerical Flux

In the case of the Maxwell's equations with constant permittivity and permeability inside each element, the numerical flux for the linear case can be derived analytically by solving a Riemann's problem with Rankine-Hugoniot jump conditions [8] along a normal $\hat{\boldsymbol{n}}$. Thus, the numerical flux difference for the three-dimensional case is [8]

$$\hat{\boldsymbol{n}}\cdot\begin{bmatrix}\vec{\boldsymbol{\mathcal{F}}}_E-\vec{\boldsymbol{\mathcal{F}}}_E^*\\ \vec{\boldsymbol{\mathcal{F}}}_H-\vec{\boldsymbol{\mathcal{F}}}_H^*\end{bmatrix}=\begin{bmatrix}-\frac{1}{\{\{Z\}\}}\frac{\hat{\boldsymbol{n}}\times(Z^+[\boldsymbol{\mathcal{H}}]+\alpha\hat{\boldsymbol{n}}\times[\boldsymbol{\mathcal{E}}])}{2}\\ \frac{1}{\{\{Y\}\}}\frac{\hat{\boldsymbol{n}}\times(Y^+[\boldsymbol{\mathcal{E}}]+\alpha\hat{\boldsymbol{n}}\times[\boldsymbol{\mathcal{H}}])}{2}\end{bmatrix}, \tag{57}$$

where

$$[\boldsymbol{u}]=\boldsymbol{u}^--\boldsymbol{u}^+,\quad\{\{\boldsymbol{u}\}\}=\frac{\boldsymbol{u}^-+\boldsymbol{u}^+}{2},$$

$$[\![\boldsymbol{u}]\!]=\hat{\boldsymbol{n}}^-\boldsymbol{u}^-+\hat{\boldsymbol{n}}^+\boldsymbol{u}^+,\quad Z^\pm=\frac{1}{Y^\pm}=\sqrt{\frac{\mu^\pm}{\epsilon^\pm}}.$$

In this notation, "$-$" represents the local element while "$+$" represents the neighboring element, as shown in Fig. 2. The upwind parameter $\alpha\in[0,1]$ ensures that the scheme is stable and convergent. Setting $\alpha=1$ represents the pure upwind flux, whereas the central flux can be recovered with $\alpha=0$.

B. Total-Field Scattered-Field Formulation

Based on the Huygen's principle, it is possible to split the computational domain into two regions: the total-field region (TFR) and scattered-field region (SFR). This technique, known as the TFSF formulation [7], is widely used in the FDTD method.

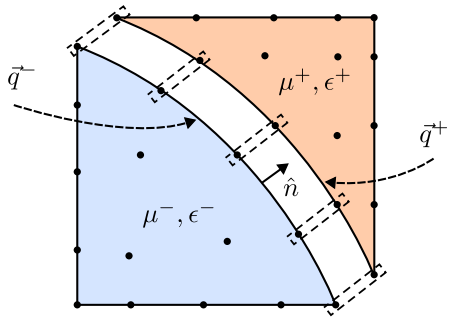

Fig. 2. Notation used for the definition of numerical fluxes. The blue element color represents the local element while the orange color represents a neighboring element.

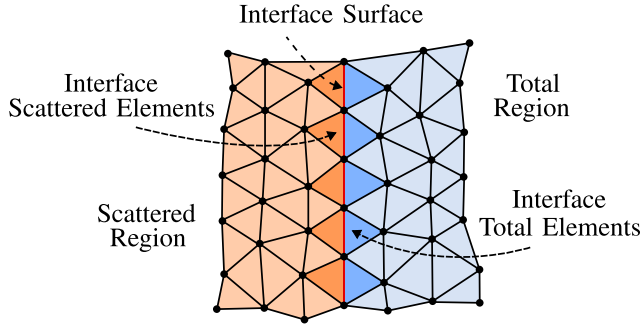

Fig. 3. Illustration of the TFSF scheme.

It relies on the linearity of Maxwell's equations and the known scattering relation

$$\vec{q}_{\text{tot}}(\boldsymbol{r},t)=\vec{q}_{\text{inc}}(\boldsymbol{r},t)+\vec{q}_{\text{scat}}(\boldsymbol{r},t), \tag{58}$$

where subscripts "tot", "scat", and "inc" indicate the total, scattered and incident, i.e., physical fields, respectively. The incident field is a known analytical expression, e.g., a plane wave. An illustration of the TFSF scheme is shown in Fig. 3.

Due to linearity, (3) is still valid in the TFR and SFR. Hence, the following equations

$$Q\frac{\partial\vec{q}_{\text{tot}}(\boldsymbol{r},t)}{\partial t}+\nabla\cdot\vec{\boldsymbol{\mathcal{F}}}(\vec{q}_{\text{tot}}(\boldsymbol{r},t),\boldsymbol{r},t)=0, \tag{59}$$

$$Q\frac{\partial\vec{q}_{\text{scat}}(\boldsymbol{r},t)}{\partial t}+\nabla\cdot\vec{\boldsymbol{\mathcal{F}}}(\vec{q}_{\text{scat}}(\boldsymbol{r},t),\boldsymbol{r},t)=0, \tag{60}$$

are solved in their respective domains. The field differences are given by

$$[\vec{q}_{\text{tot}}(\boldsymbol{r},t)]=\vec{q}_{\text{tot}}^-(\boldsymbol{r},t)-\vec{q}_{\text{tot}}^+(\boldsymbol{r},t), \tag{61}$$

$$[\vec{q}_{\text{scat}}(\boldsymbol{r},t)]=\vec{q}_{\text{scat}}^-(\boldsymbol{r},t)-\vec{q}_{\text{scat}}^+(\boldsymbol{r},t). \tag{62}$$

As long as the local element is within TFR or SFR, the evaluation is straightforward. The only change happens in the interface elements sharing a face with the TFSF interface, as indicated in Fig. 3. If the local element is in the TFR, the field difference is updated to

$$[\vec{q}(\boldsymbol{r},t)]_{\text{tot}}=\vec{q}_{\text{tot}}^-(\boldsymbol{r},t)-\vec{q}_{\text{scat}}^+(\boldsymbol{r},t)-\vec{q}_{\text{inc}}(\boldsymbol{r},t), \tag{63}$$

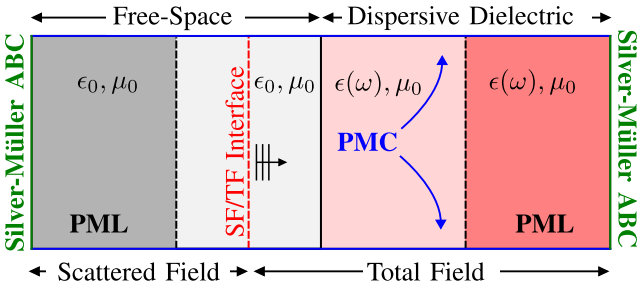

Fig. 4. Illustration of the two-dimensional case study.

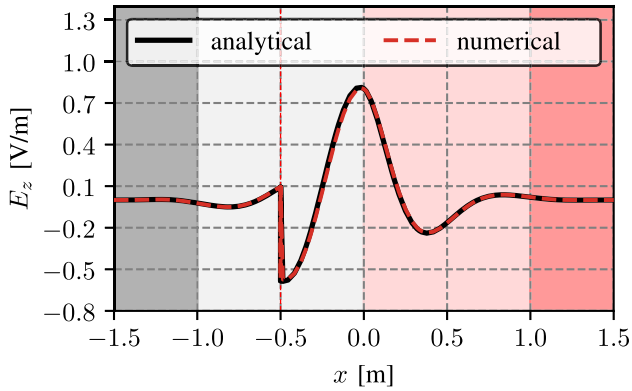

Fig. 5. Electric field with 6th order elements at $t = 7\tau$ and $1/6\lambda_c$ mesh.

while if the local element is within the SFR

$$[\vec{q}(\boldsymbol{r},t)]_{\text{scat}} = \vec{q}^{-}_{\text{scat}}(\boldsymbol{r},t) - \vec{q}^{+}_{\text{tot}}(\boldsymbol{r},t) + \vec{q}_{\text{inc}}(\boldsymbol{r},t). \tag{64}$$

This formulation has the requirement that all electromagnetic fields must approach zero at $t = 0$ everywhere [21].

IV. Numerical Results

This section validates the formulation by applying it to a two-dimensional canonical problem that covers all previously described scenarios, confirming its accuracy and reliability. Subsequently, the formulation is tested on a more complex three-dimensional problem to demonstrate its effectiveness in addressing intricate scenarios.

The explicit fourth-order Runge-Kutta method is used for time integration, with the time step based on the minimum nodal distance [8]. Simplexes (triangles in 2D and tetrahedra in 3D) are chosen as grid elements. The upwind scheme is used for numerical flux and boundary conditions are integrated into the flux calculation [8].

A. Two-Dimensional Scattering Problem

The proposed formulation is validated by analyzing the propagation of a TMz plane wave with normal incidence into a region containing dispersive dielectric media. This setup covers all possible scenarios: a PML truncating free space, free space itself, dispersive dielectric media, and a PML truncating the dispersive media, as shown in Fig. 4. In the simulation, the incident field is given by

$$\boldsymbol{\mathcal{E}}_{\text{inc}}(\boldsymbol{r},t) = g\left(t - \sqrt{\epsilon_0\mu_0}\,\hat{\boldsymbol{x}}\cdot\boldsymbol{r}\right)\hat{\boldsymbol{z}}, \tag{65}$$

$$\boldsymbol{\mathcal{H}}_{\text{inc}}(\boldsymbol{r},t) = \sqrt{\frac{\epsilon_0}{\mu_0}}\hat{\boldsymbol{x}} \times \boldsymbol{\mathcal{E}}_{\text{inc}}(\boldsymbol{r},t), \tag{66}$$

where $g(t)$ is the cosine-modulated Gaussian waveform

$$g(t) = \cos(2\pi f_c t)\exp\left(-t^2/\tau^2\right), \tag{67}$$

with f_c being its center frequency and τ representing its time constant. To analyze a frequency band from 100 MHz to 500 MHz, f_c was set to 300 MHz and τ was set to $0.8/f_c$ seconds. To ensure that the electromagnetic fields were zero at both the start and end of the simulation, a time delay of 7τ was applied, and the fields were simulated for a total duration of 20τ. A single Lorentz pole was used to model the dispersive dielectric media with its parameters set to $\omega_1 = 1.25 \times 2\pi f_c$, $\delta_1 = 0.3 \times \omega_1$, $\Delta\epsilon = 2.5$ and $\epsilon_\infty = 1$ [9]. The computational domain of size $3\lambda_c \times 2\lambda_c$ was considered, where λ_c is the wavelength of the central frequency. The mesh size was set to $1/6\lambda_c$ and $1/12\lambda_c$, resulting in a total of 570 and 2070 elements, respectively. The PML profile was a second-degree polynomial with parameters chosen to achieve an attenuation of 72 dB within the PML. The geometric dimensions and the electric field at a cross-section along the propagation direction are shown in Fig. 5.

To evaluate the impact of the frequency dependence of the dispersive dielectric media in the simulation, the relative L_2 error was calculated as

$$\text{L}_2 \text{ Error} = \sqrt{\frac{\int_\Omega ||\mathbf{E}^{\text{n}} - \mathbf{E}^{\text{a}}||^2 d\Omega}{\int_\Omega ||\mathbf{E}^{\text{a}}||^2 d\Omega}}, \tag{68}$$

with a representing the analytical and n the numerical results. This error is determined by taking the Fourier transform of the electric field from the time-domain numerical solution and comparing it to the frequency-domain analytical solution, weighted by the incident field's frequency components.

Fig. 6 shows how the error across the frequency band of interest changes with varying element orders. The gray area represents the frequency spectrum of the incident field. The parabolic trend observed at lower frequencies is related to the intensity of the incident field at those frequencies. As the frequency moves away from the center frequency, the spectral energy decreases, leading to a reduction in the denominator of (68). The error also gradually increases with frequency due to numerical grid dispersion. As frequency rises, the spatial sampling rate (number of elements per wavelength) decreases, resulting in increased mesh dispersion. Fig. 7 shows the convergence rate of the L_2 error at the center frequency 300 MHz with varying element orders. It was observed that doubling the mesh density reduced the overall error by 20 dB with only minor variations in the spectrum.

B. Three-Dimensional Scattering Problem

The next problem involves the electromagnetic scattering of a plane wave by a dispersive dielectric sphere, as illustrated in Fig. 8. The material properties of the sphere were determined

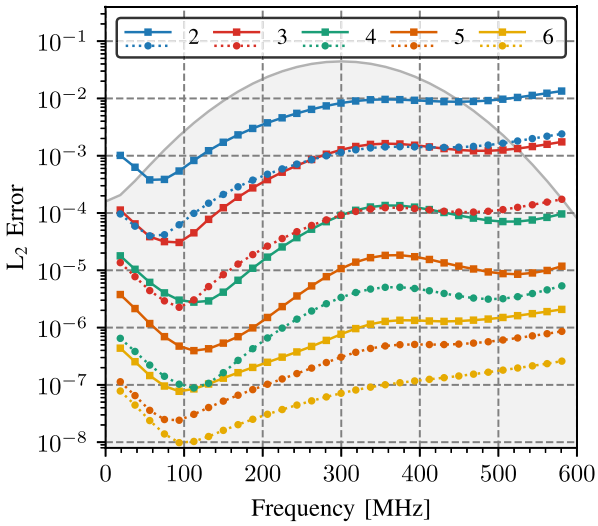

Fig. 6. L_2 error of the electric field varying the order of the elements.

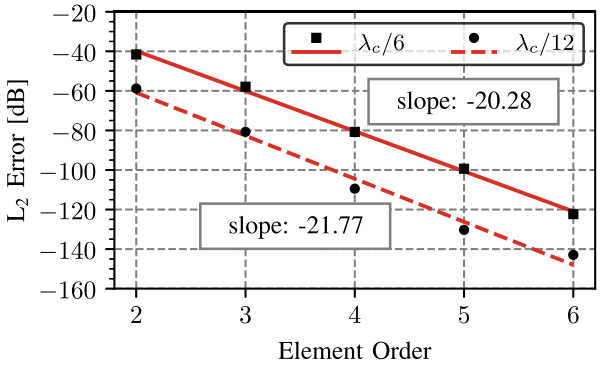

Fig. 7. Convergence rate of the L_2 error varying element orders at 300 MHz.

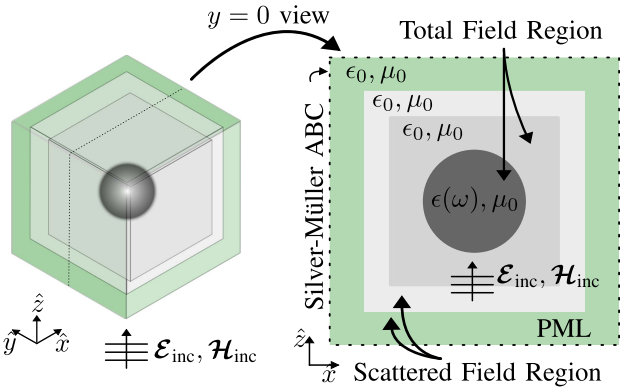

Fig. 8. Illustration of the three-dimensional case study.

using vector fitting with data from [22] for silver across the frequency range of 30 THz to 1200 THz. In contrast to [9], which employed six conjugate poles, a satisfactory approximation was achieved with only three conjugate poles through Basin-hopping combined with non-linear least squares optimization. The poles and residues of the fitted model are illustrated in Fig. 9, and their values are listed in Table I.

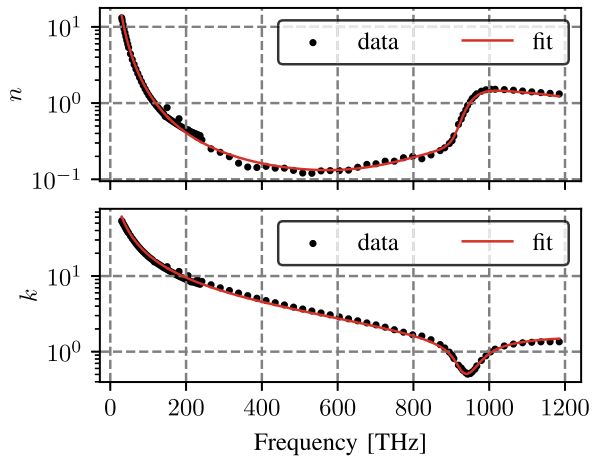

Fig. 9. Fitting of the refractive index n and extinction coefficient k of silver over the frequency range from 30 THz to 1200 THz.

TABLE I
POLES AND RESIDUES OF THE FITTED MODEL

Residues	Poles
$+0.27 + 2931j$	$-0.03 - 0.01j$
$-29.39 + 212j$	$-18.60 - 3.75j$
$+1.10 + 0.61j$	$-0.37 - 4.20j$

The simulation was performed with a plane wave propagating in the z direction and the electric field polarized along x. To analyze the time-domain response, considering the frequency response of the material between 100 THz and 500 THz, the central frequency, f_c, was set to 300 THz, with $\tau = 0.8/f_c$ seconds. A time delay of 7τ was applied to ensure that the electromagnetic fields were zero at the start of the simulation. The total duration of the simulation was also 7τ seconds, which corresponds to the time when the electromagnetic incident field reaches its peak value. The computational domain had dimensions of $1.5\lambda_c \times 1.5\lambda_c \times 1.5\lambda_c$, where λ_c represents the wavelength at the center frequency. The mesh size within the sphere was set to $1/15\lambda_c$, and up to $1/4\lambda_c$ within the PML, resulting in a total of 4752 elements. The PML employed a second-degree polynomial profile, with parameters chosen to achieve an attenuation of 36 dB. The width of the PML was $0.25\lambda_c$, the width of the scattering region (excluding the PML) was $0.125\lambda_c$, and the radius of the sphere was $0.25\lambda_c$.

The absolute value of the electric field at the $y = 0$ plane is shown in Fig. 10 while the normalized error at two different planes, absolute difference between the numerical solution and the analytical solution [23] (with 50 terms) normalized by the amplitude the incident field, is shown in Fig. 11 using 4th order elements. The error is concentrated near the surface of the sphere, as illustrated in Fig. 11(a). This discrepancy is attributed to the limited discretization of the sphere, which has a significant impact on the accuracy of the near field. Taking into account these factors, the relative L_2 error was computed at the TFSF interface, yielding a value of 1.04% with 4th order elements. The normalized error at one of the faces of the cube containing the TFSF interface is shown in Fig. 11(b). This finding indicates

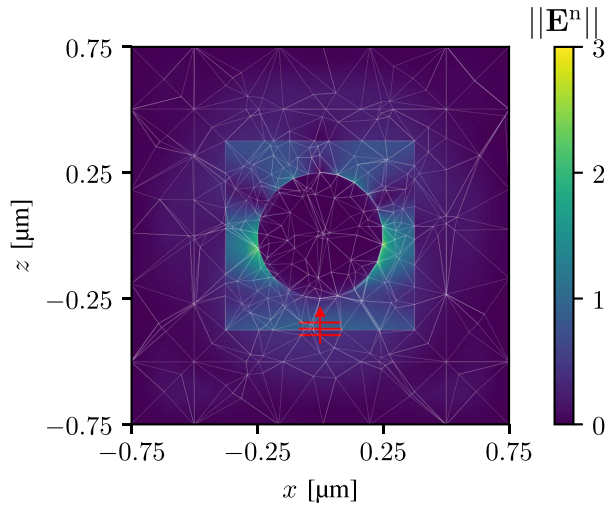

Fig. 10. Absolute value of the electric field at the $y = 0$ plane at $t = 7\tau$ using 4th order elements.

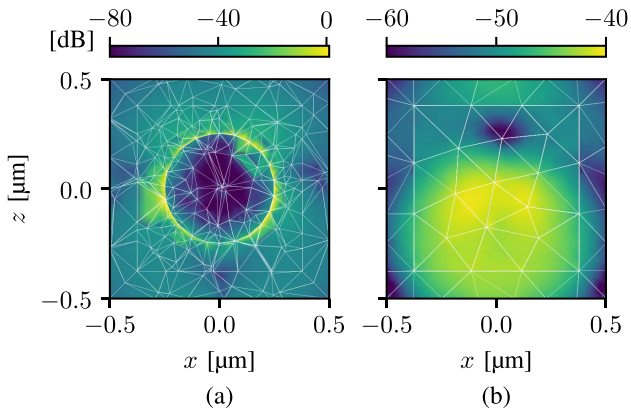

Fig. 11. Normalized error $||\boldsymbol{\mathcal{E}}^{\mathrm{n}} - \boldsymbol{\mathcal{E}}^{\mathrm{a}}||/E_0$ of the electric field at $t = 7\tau$ using 4th order elements at (a) $y = 0$ and (b) $y = -0.375\lambda_c$, excluding the PML, where E_0 is the amplitude of the incident field. The error slightly above 0 dB in (a) occurs only at elements intersecting the sphere due to rapid electric field changes and discretization, unlike (b), where the error stays below −40 dB.

a strong agreement between the numerical and analytical solutions, especially considering the notable variation in permittivity of the material analyzed.

V. Conclusion

This work has presented a new formulation of the DGTD method applied to electromagnetic scattering problems involving general dispersive media modeled by vector fitting. The main contribution is enabling direct truncation of dispersive materials without the need for a region of simple dielectric between the scatterer and the PML by extending the uniaxial PML to handle general dispersive media based on the CCPR model. The formulation's modularity allows for flexible and efficient adaptation to various problem types, activating dispersive and/or PML components as needed. Numerical results for two-dimensional and three-dimensional scattering problems demonstrate excellent agreement with analytical solutions, showcasing the accuracy and flexibility of the proposed method.

References

[1] P. Li and L. J. Jiang, "Uncertainty quantification for electromagnetic systems using ASGC and DGTD method," *IEEE Trans. Electromagn. Compat.*, vol. 57, no. 4, pp. 754–763, Aug. 2015.
[2] P. Li, Y. Shi, L. J. Jiang, and H. Bağcı, "DGTD analysis of electromagnetic scattering from penetrable conductive objects with IBC," *IEEE Trans. Antennas Propag.*, vol. 63, no. 12, pp. 5686–5697, Dec. 2015.
[3] S. Yan and J.-M. Jin, "A dynamic p-adaptive DGTD algorithm for electromagnetic and multiphysics simulations," *IEEE Trans. Antennas Propag.*, vol. 65, no. 5, pp. 2446–2459, May 2017.
[4] H. Bao, L. Kang, S. D. Campbell, and D. H. Werner, "PML implementation in a nonconforming mixed-element DGTD method for periodic structure analysis," *IEEE Trans. Antennas Propag.*, vol. 67, no. 11, pp. 6979–6988, Nov. 2019.
[5] H. H. Zhang, X. Y. Liu, Y. Liu, Z. C. Fan, and H. L. Du, "Thermal-mechanical-electromagnetic multiphysics simulation of satellite phased array antenna based on DGTD and FEM method," *IEEE J. Multiscale Multiphys. Comput. Tech.*, vol. 9, pp. 236–246, 2024.
[6] J.-M. Jin, *The Finite Element Method in Electromagnetics*, 3rd ed. Hoboken NJ, USA: Wiley, 2014.
[7] A. Taflove and S. C. Hagness, *Computational Electrodynamics: The Finite-Difference Time-Domain Method*, 3rd ed. Norwood, MA, USA: Artech House, 2005.
[8] J. S. Hesthaven and T. Warburton, *Nodal Discontinuous Galerkin Methods* (Texts in Applied Mathematics Series). vol. 54. New York, NY, USA: Springer, 2008.
[9] M. Han, R. W. Dutton, and S. Fan, "Model dispersive media in finite-difference time-domain method with complex-conjugate pole-residue pairs," *IEEE Microw. Wireless Compon. Lett.*, vol. 16, no. 3, pp. 119–121, Mar. 2006.
[10] W. Mai et al., "Prismatic discontinuous Galerkin time domain method with an integrated generalized dispersion model for efficient optical metasurface analysis," *Opt. Mater. Exp.*, vol. 10, no. 10, pp. 2542–2559, 2020.
[11] Q. Ren, H. Bao, S. D. Campbell, L. J. Prokopeva, A. V. Kildishev, and D. H. Werner, "Continuous-discontinuous Galerkin time domain (CDGTD) method with generalized dispersive material (GDM) model for computational photonics," *Opt. Exp.*, vol. 26, no. 22, pp. 29005–29016, 2018.
[12] T. Lu, P. Zhang, and W. Cai, "Discontinuous Galerkin methods for dispersive and lossy Maxwell's equations and PML boundary conditions," *J. Comput. Phys.*, vol. 200, no. 2, pp. 549–580, 2004.
[13] L. D. Angulo, J. Alvarez, M. F. Pantoja, S. G. Garcia, and A. Bretones, "Discontinuous Galerkin time domain methods in computational electrodynamics: State of the art," *Forum Electromagn. Res. Methods Appl. Technol.*, vol. 10, no. 4, pp. 1–24, 2015.
[14] J.-P. Berenger, "A perfectly matched layer for the absorption of electromagnetic waves," *J. Comput. Phys.*, vol. 114, no. 2, pp. 185–200, 1994.
[15] F. L. Teixeira, W. C. Chew, M. Straka, M. Oristaglio, and T. Wang, "Finite-difference time-domain simulation of ground penetrating radar on dispersive, inhomogeneous, and conductive soils," *IEEE Trans. Geosci. Remote Sens.*, vol. 36, no. 6, pp. 1928–1937, Nov. 1998.
[16] B. Gustavsen and A. Semlyen, "Rational approximation of frequency domain responses by vector fitting," *IEEE Trans. Power Del.*, vol. 14, no. 3, pp. 1052–1061, Jul. 1999.
[17] K. Niknam and J. J. Simpson, "A review of grid-based, time-domain modeling of electromagnetic wave propagation involving the ionosphere," *IEEE J. Multiscale Multiphys. Comput. Tech.*, vol. 6, pp. 214–228, 2021.
[18] X. Qin, X. Wu, S. Wang, X. Zhao, Y. Zhou, and Q. Ren, "Perfectly matched layer for cole-cole dispersive media in DGTD method," *IEEE J. Multiscale Multiphys. Comput. Tech.*, vol. 9, pp. 320–329, 2024.
[19] Q. Ren, H. Cao, and Q. H. Liu, "Novel efficient discontinuous Galerkin time-domain modeling of dispersive chiral metamaterials via media homogenization," *IEEE Trans. Microw. Theory Techn.*, vol. 72, no. 9, pp. 5218–5227, Sep. 2024.
[20] J. S. Hesthaven and T. Warburton, "Nodal high-order methods on unstructured grids: I time-domain solution of Maxwell's equations," *J. Comput. Phys.*, vol. 181, no. 1, pp. 186–221, 2002.
[21] K. Busch, M. König, and J. Niegemann, "Discontinuous Galerkin methods in nanophotonics," *Laser Photon. Rev.*, vol. 5, no. 6, pp. 773–809, 2011.
[22] E. D. Palik, *Handbook of Optical Constants of Solids*, vol. 3. Cambridge, MA, USA: Academic, 1998.
[23] J.-M. Jin, *Theory and Computation of Electromagnetic Fields*, 2nd ed. Hoboken, NJ, USA: Wiley, Aug. 2015.